Controlling nucleation and growth of nanodroplets in supersonic nozzles

Kiril A. Streletzky, Yury Zvinevich,[a] and Barbara E. Wyslouzil
Department of Chemical Engineering, Worcester Polytechnic Institute, Worcester, Massachusetts 01609-2280

Reinhard Strey
Institute for Physical Chemistry, University of Cologne, Cologne, Germany

(Received 14 August 2001; accepted 3 December 2001)

We present the first results for a new supersonic nozzle that decouples nucleation and droplet growth, and closely controls the supersaturation and temperature during nucleation. We characterize the expansions using pressure trace measurements, and the aerosol properties using light scattering and small angle neutron scattering. We show that when nucleation and droplet growth are separated, the aerosol number density decreases, the average particle size increases, and the aerosol can be more monodisperse than that formed in a conventional nozzle. Under these conditions, we can estimate the nucleation rate J as a function of supersaturation S and temperature T directly from the experimental data. For D_2O we find that the nucleation rate is $4.3\times10^{15}\leqslant J/\mathrm{cm}^{-3}\ \mathrm{s}^{-}\leqslant 6.0\times10^{15}$ at $230.1\leqslant T/K\leqslant 230.4$ and $29.2\leqslant S\leqslant 32.4$. © *2002 American Institute of Physics.*
[DOI: 10.1063/1.1446031]

I. INTRODUCTION

Particle formation and growth in supersonic expansions occur in many natural and technological applications.[1] Volcanic eruptions, for example, produce sulfate aerosol which can profoundly influence both stratospheric chemistry and radiative processes.[2] Aerosol formation and growth in turbomachinery, on the other hand, decrease turbine efficiency and can erode turbine blades.[3,4] Thus, understanding condensation in supersonic flows is important for predicting, and possibly controlling, when the phase transition will occur under the high supersaturations achieved in these rapid expansions. Direct nucleation and growth rate measurements are critical for testing and developing the basic physical models describing these phenomena.[5,6] These models, in turn, help us create accurate descriptions of atmospheric and industrial processes.

Laval nozzles have been used extensively to examine condensation[7–9] of both mixtures of condensible vapor in a carrier gas[10–25] and pure vapors,[26–30] especially steam.[27–29] In conventional Laval nozzles, the cross-sectional flow area first decreases to the throat and then increases monotonically in the supersonic region. As the gas flows through the nozzle it expands and the temperature falls at a rate of $\sim 10^6$ K/s. Because the equilibrium vapor pressure decreases exponentially with temperature, very high supersaturations can be achieved. Eventually, however, homogeneous nucleation produces enough new particles that their growth rapidly depletes the condensible vapor and quenches further particle formation. Experimentally, the onset of condensation in a supersonic nozzle is determined either by observing when the heat released to the flow by the phase transition causes a noticeable deviation of a state variable from its isentropic value,[12,24] or by detecting light scattered by the aerosol.[27,28] Because onset is the result of nucleation and growth taking place simultaneously over a wide range of temperature and supersaturation, onset measurements alone do not directly yield information about droplet nucleation and growth rates. The information about these processes is only obtained indirectly by modeling the system.[1,28]

To address these limitations, we are developing supersonic nozzles that decouple droplet nucleation and growth. Ideally, nucleation should occur at constant temperature T and supersaturation S over a well defined time interval Δt. Given such a nozzle, we can then use small angle neutron scattering (SANS) to measure the number density N of the aerosol,[31–34] and, thus, determine the nucleation rate J directly as $J(S,T)=N/\Delta t$. Droplets formed under these conditions can be more monodisperse than droplets formed during spontaneous condensation in a conventional nozzle. Monodisperse aerosols are themselves of technological interest,[35] and they have the added advantage that the SANS scattering spectra have more structure and are easier to interpret.

In this paper we present the first results of our efforts to build and work with such nozzles. In particular, we discuss the design and characterization of the new nozzles using conventional thermodynamic state measurements, the optimization of the operating conditions using pressure trace and light scattering measurements, the particle size distribution measurements using SANS, the variation in aerosol size distribution as a function of operating conditions, and the degree to which nucleation and growth can be separated. We also estimate the characteristic time for nucleation Δt, the nucleation rate J, and the corresponding supersaturation S and temperature T. Finally, we combine the light scattering and SANS results to estimate the droplet growth rate in the nozzle.

II. NOZZLE DESIGN

The concept of a supersaturation pulse is central to all quantitative nucleation rate measurements, and the technique

[a]Permanent address: Institute of Physics, National Academy of Sciences of Belarus, Minsk, Belarus.

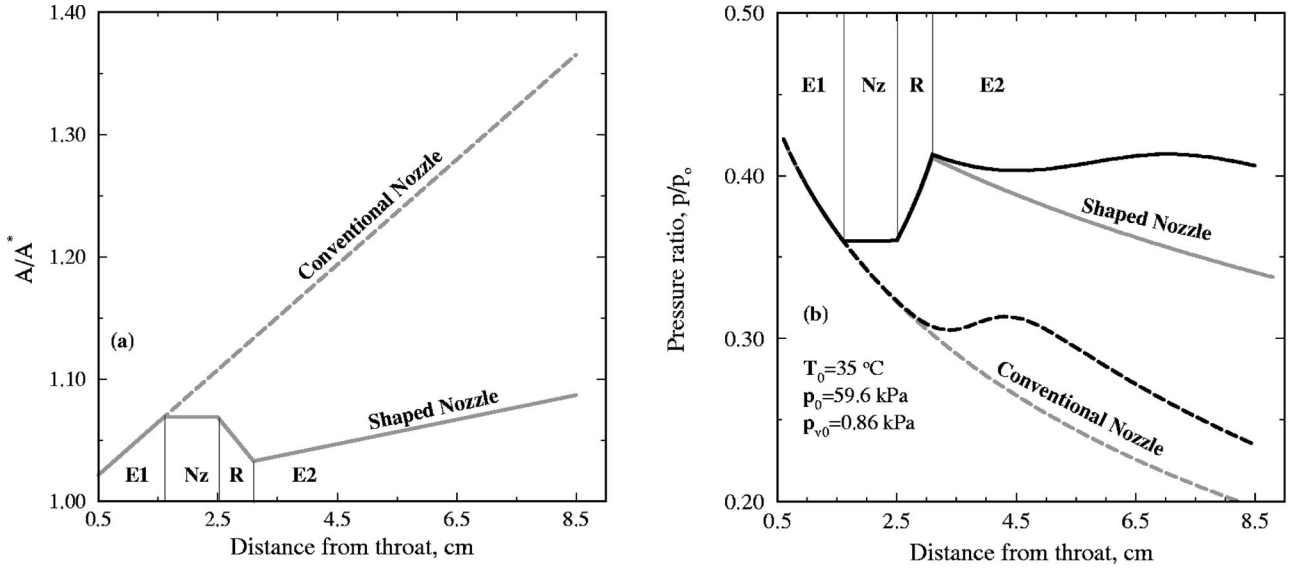

FIG. 1. The four zones in the shaped nozzle are indicated as E1, the first expansion; Nz, the nucleation zone; R, the recompression; and E2, the second expansion. (a) The profile of the conventional nozzle (dashed gray) is much simpler than that of the ideal shaped nozzle (solid gray). (b) In both nozzles, the pressure trace for the dilute D_2O–N_2 mixture (solid or dashed black line) follows the isentropic expansion (solid or dashed gray line) closely up to the onset of condensation. Although onset occurs at about the same distance downstream of the throat, the pressure and temperature are quite different. The conditions used as input to the model are noted in the figure.

has been implemented in many of the expansion devices used to study vapor-to-liquid nucleation. In expansion cloud chambers,[36–38] shock tubes,[39] piston-expansion tubes,[40] and wave tubes,[41,42] the pressure decreases rapidly as a function of time until it reaches a minimum value. The pressure is maintained at this minimum value for a short time (0.3–10 ms), and then a rapid recompression is applied to produce a slightly higher pressure in the system. When the system is at its lowest pressure, the supersaturation and the nucleation rate are maximized. The slight increase in pressure raises the temperature and reduces the supersaturation enough to effectively stop nucleation, while allowing existing particles to grow rapidly.[36,38]

Our objective is to build a supersonic nozzle with a spatial profile such that a fluid element moving through the nozzle experiences the same pressure history as vapor undergoing a controlled pressure pulse. Thus, in the shaped nozzle, the first expansion is produced by the initial increase in the area ratio after the throat. This is followed by the nucleation zone where the area ratio is constant, a short recompression region where the area ratio contracts, and finally by a second expansion region. Figure 1(a) compares the area ratio for an ideal shaped nozzle to that of a conventional nozzle. The gentle expansion after the recompression in the shaped nozzle prevents the flow from shocking back to the subsonic regime as heat is added by the phase transition.

In our preliminary design, we assume that the flow in our slender, gently expanding nozzles is one dimensional. For an isentropic expansion in a conventional nozzle, the pressure ratio p/p_0 and the temperature ratio T/T_0 are related to the Mach number M by[43]

$$\frac{p}{p_0}=\left[1+\frac{\gamma-1}{2}M^2\right]^{\gamma/(\gamma-1)} \tag{1}$$

and

$$\frac{T_0}{T}=1+\frac{\gamma-1}{2}M^2, \tag{2}$$

where γ is the ratio of the constant pressure and constant volume heat capacities, and the subscript 0 refers to the conditions when the fluid is at rest. The Mach number is related to the area ratio (A/A^*) by

$$\frac{A}{A^*}=\frac{1}{M}\left[\frac{2+(\gamma-1)M^2}{\gamma+1}\right]^{(\gamma+1)/(2\gamma-2)}, \tag{3}$$

where A^* is the cross-sectional area of the nozzle throat. In the shaped nozzle, recompression of the supersonic flow is carried out by a series of shocks emanating from the walls of the nozzle. As long as the shocks are weak, the flow remains isentropic and Eqs. (1)–(3) are still valid.[43] The gray lines in Fig. 1(b) are the pressure profiles, calculated using Eqs. (1) and (3), that correspond to the isentropic expansion of pure N_2 for the two nozzle shapes illustrated in Fig. 1(a). In the conventional nozzle $d(A/A^*)/dx$ is constant and the pressure drops monotonically. In the supersonic region of the shaped nozzle, the pressure profile mirrors the behavior of A/A^* and closely matches the pressure history found in other expansion devices.

To estimate reasonable operating conditions, we then modeled condensation in the nozzle for a mixture of condensible and noncondensible gas assuming steady, one-dimensional, inviscid flow.[10,21,34] For every step in the expansion, Δx, we calculate the number density of newly formed droplets, ΔN, using the steady state classical nucleation rate[44] and the local gas velocity. The condensate mass fraction g at every position along the flow is calculated using an isothermal growth law.[39] From g and the latent heat of vaporization of the condensate, we obtain the other properties of the condensing flow by solving the diabatic flow

equations[21,24] for the given nozzle shape. The physical property correlations for D_2O used in the modeling are those of Wölk.[45]

The black curves in Fig. 1(b) illustrate the predicted pressure traces for the flow of a dilute mixture of D_2O in N_2 through both the conventional and the shaped nozzle. In this example, the stagnation conditions were $T_0=308.2\,\mathrm{K}$ and $p_0=59.6\,\mathrm{kPa}$, and the partial pressure of condensible was $p_{v0}=861\,\mathrm{Pa}$. In the conventional nozzle, the pressure trace for the condensing flow follows that of the pure N_2 expansion until particle growth releases enough heat to produce a rapid deviation in pressure from the isentrope at the onset of condensation. Modeling suggests that nucleation is significant for some distance both upstream and downstream of onset, and, thus, occurs over a wide range of temperature and supersaturation. In the shaped nozzle, the pressure trace of the condensing flow follows the corresponding isentrope closely both through the nucleation zone and the recompression region. Only at the end of the recompression region does the condensing flow curve separate from its isentrope. In this case, modeling shows that most particle formation is restricted to the nucleation zone, and that nucleation and droplet growth are effectively decoupled. As long as there is no noticeable condensation in the nucleation zone, the temperature is related to the pressure by

$$\frac{T}{T_0}=\left(\frac{p}{p_0}\right)^{(\gamma_m-1)/\gamma_m}, \tag{4}$$

where γ_m is the ratio of heat capacities for the mixture of carrier gas and condensible. The supersaturation is given by

$$S=\frac{p_v}{p_{\mathrm{eq}}(T)}=\frac{p_{v0}}{p_{\mathrm{eq}}(T)}\frac{p}{p_0}, \tag{5}$$

where p_v and p_{v0} are the local and initial partial pressures of condensible and $p_{\mathrm{eq}}(T)$ is the equilibrium vapor pressure at the local temperature. Modeling also suggests that if the second expansion were missing from the shaped nozzle, the rapid heat addition due to particle growth after the compression would frequently produce a shock. Downstream of the shock, the flow would be subsonic, the temperature would increase, and the droplets would evaporate.

As with other expansion devices, each shaped nozzle has a limited range of operating conditions. If the initial partial pressure of the condensible species p_{v0} is too high, spontaneous condensation occurs upstream of the controlled nucleation zone. If p_{v0} is too low, too few droplets form in the nucleation zone to grow and deplete the vapor before an uncontrolled burst of nucleation occurs in the second expansion. Under ideal conditions, however, most of the droplets form in the nucleation zone, at constant temperature and supersaturation, the newly formed droplets grow rapidly enough to deplete the vapor and suppress further particle formation, and the second expansion absorbs enough heat to prevent a shock back to subsonic flow.

Figure 2 depicts the predicted aerosol size distributions 7.0 cm downstream of the throat. We see that the shaped nozzle produces an aerosol with droplets of larger average size and lower number density than the conventional nozzle. Furthermore, the constant nucleation rate in the nucleation zone produces a constant number density near the maximum. These observations are consistent with the idea that in order to control nucleation the nucleation rate in the shaped nozzle must be lower than the peak rates that occur during a spontaneous condensation event. In this example, nucleation rates in the shaped nozzle are 2–3 orders of magnitude lower than the peak values reached in the conventional nozzle. The lower nucleation rates in the shaped nozzle mean that fewer nuclei compete for the available vapor and each droplet grows larger. A simple volume balance shows that $\langle r^3\rangle$ is proportional to the amount of condensible entering the system divided by the number of droplets. Although both size distributions illustrated in Fig. 2 have similar absolute widths, the size distribution of the aerosol formed in the shaped nozzle is more monodisperse than that formed in the conventional nozzle in the sense that $\sigma_r/\langle r\rangle$ is smaller, where here we define σ_r as the width of the size distribution when N is 1% of the maximum value. Physically, σ_r is determined by the length of time over which nucleation is significant. For the conditions chosen here, this time is about the same in both nozzles.

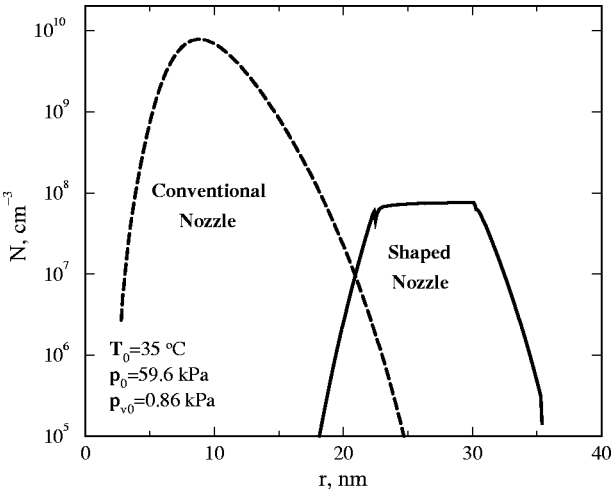

FIG. 2. The aerosol produced in the shaped nozzle has a much lower number density of larger particles compared to the aerosol formed in the conventional nozzle. Both size distributions correspond to a location 7 cm downstream of the throat. In the shaped nozzle the droplets are still growing significantly while those in the conventional nozzle are not.

The shaped nozzles are otherwise identical to our conventional nozzles described earlier.[24,31] The flow area is rectangular with flat side walls, and the upper and lower blocks are machined to define the area ratio. At the throat the height of the channel is 5 mm, the width is 12.7 mm, and the nominal value of A^* is 63.5 mm^2. Neoprene gaskets constrained in O-ring grooves seal the nozzle. Glass or Si windows in the sidewalls allow transmission of light or neutrons, respectively. One difficulty encountered in implementing the ideal design is that the area ratio of a nozzle derived from pressure measurements always differs from the physical area ratio due to the growth of boundary layers along the nozzle walls. This problem is compounded in the recompression region where boundary layers grow more rapidly than in the expanding region of the flow.[43] Based on our experience with other nozzles, we altered the geometric area ratio to try and com-

pensate for this effect and better match the desired pressure profile.

III. EXPERIMENTAL METHODS

A. Aerosol production

A detailed description of the experimental apparatus used to produce the stable supersonic flow is given in Wyslouzil *et al.*[24] Here we simply outline the basic components and the operating principles. The expanding gas is a dilute (<2 mol %) mixture of D_2O in N_2 carrier gas. We use D_2O rather than H_2O because the neutron scattering signal, which depends on the scattering length density squared, is 144 times greater for a D_2O aerosol than for an identical H_2O aerosol. We generate a large flow (~5.5 g/s) of N_2 by evaporating liquid N_2 in a commercial heat exchanger using room air as the heat source. A second stream of hot N_2 gas (~3 g/s) entrains and evaporates a metered stream of D_2O droplets. After the carrier gas and the vapor-rich gas streams are mixed, they flow through a second heat exchanger to adjust the temperature. The combined flow then enters the plenum where final temperature equilibration takes place and the stagnation pressure p_0 and temperature T_0 are measured. The mixture then expands through the nozzle and is exhausted to the atmosphere by two rotary vane vacuum pumps.

Most of the experimental results presented here are correlated with the condensible mass flow rate $\dot{m}_v$ entering the system because this is the experimentally measured variable. For modeling, and to compare with other experimental results, we also calculate the partial pressure of the condensible.[24] Under stagnation conditions the partial pressure of condensible for our dilute mixtures is given by

$$p_{v0}=\frac{\dot{m}_v/\mu_v}{\dot{m}_i/\mu_i}p_0, \tag{6}$$

where μ_v and μ_i are the molecular weights of the condensible and inert carrier gas, respectively, and $\dot{m}_i$ is the mass flow rate of the carrier gas. At $T_0=35.0\,^{\circ}\mathrm{C}$ and $p_0=59.6\,\mathrm{kPa}$, the mass flow rate of N_2 through the nozzle was 488 g/min corresponding to a molar flow rate of 17.4 mol/min.

B. Characterizing the supersonic expansion

The gas dynamics of steady one-dimensional flow in supersonic nozzles is well understood[43] and all the properties of the flow can be derived from the initial gas phase composition, two stagnation conditions, temperature T_0 and pressure p_0, for example, and one state variable as a function of position [e.g., $p(x)$]. In the absence of condensation, Eqs. (1)–(3) are valid, and, thus, expansions of pure N_2 define the effective area ratio and calibrate the shape of the nozzle. When condensation occurs in the nozzle, the remaining variables (gas density, velocity, temperature) can be derived from the effective area ratio, the measured state variables, and an equation of state for the gas, by integrating the diabatic flow equations.[21,24] As in our previous work, we define the onset of condensation in terms of a temperature difference between the condensing flow curve, T_{cf}, and the isentropic expansion of a gas with the same properties as the mixture, T_{mi}. Our onset criterion is $T_{cf}-T_{mi}=0.5\,\mathrm{K}$. The major difference between the current experiments and those described earlier[24] is that we have decreased the size of the static pressure probe to 1.27 mm in diameter, to reduce its influence on the flow field.

C. Characterizing the aerosol

Although thermodynamic state measurements determine the onset of condensation in the nozzle, they do not provide direct information about the particle size distribution of the aerosol. Aerosol measurement methods that require sampling from the flow are not feasible in our experiments because the droplets evaporate as soon as the flow decelerates. Thus, we use two *in situ* techniques, light scattering and small angle neutron scattering (SANS), to characterize the aerosol.

1. Light scattering experiments

Light scattering experiments are useful for detecting the onset of condensation under conditions where state variable measurements are difficult,[19] and they can be used to estimate the number density and average size of the droplets formed in supersonic expansions.[1,13] The problem inherent in the latter is that the average size of the droplets formed in supersonic expansions ($\langle r\rangle\sim 1-20\,\mathrm{nm}$) is generally much smaller than the wavelength of visible light ($\lambda\approx 400-600$ nm). In the Rayleigh limit, $\langle r\rangle/\lambda\ll 1$, the intensity of the scattered light I_0 is proportional to $N\langle r^6\rangle$ and is independent of the observation angle. As a result, the parameters of the particle size distribution cannot be deduced from the scattering signal without additional information. The usual approach[1,13] is to use the pressure data to infer the total heat release per unit volume to the flowing gas stream, a quantity that is proportional to $N\langle r^3\rangle$. Combined with assumptions about the general shape (Gaussian or log-normal) and width of the size distribution, and the latent heat of the condensate, the two measurements together yield values for $\langle r\rangle$ and N.

We use light scattering as a way to determine the optimum operating conditions for the nozzle that is independent of the pressure trace measurements. As illustrated in Fig. 2, the droplet number density of the aerosol decreases and the average particle size increases when nucleation and growth are decoupled. Since I_0 is proportional to $N\langle r^6\rangle$, the light scattering signal is extremely sensitive to small changes in $\langle r\rangle$. For example, if two monodisperse aerosols have the same volume fraction and N decreases by a factor of 2, the average particle size increases by a factor $\sqrt[3]{2}$ and I_0 doubles.

To conduct the light scattering experiments, we place glass windows in the side blocks and remove the pressure probe. The internal surfaces of the nozzle are painted black and all experiments are done in the dark. Light from a 15 mW He–Ne laser ($\lambda=632.8$ nm) with a 0.8 mm beam diameter is intensity modulated by chopping the beam at 70 Hz. The beam is then split, and one beam is sent to a power meter to measure the output power of the incident radiation. The second beam enters the nozzle from the downstream side and illuminates the centerline of the flow. The collection optics are located on a movable platform beside the nozzle and collect the light scattered at 90° to the incident beam. A 5 mm wide slit defines the length of the scattering volume.

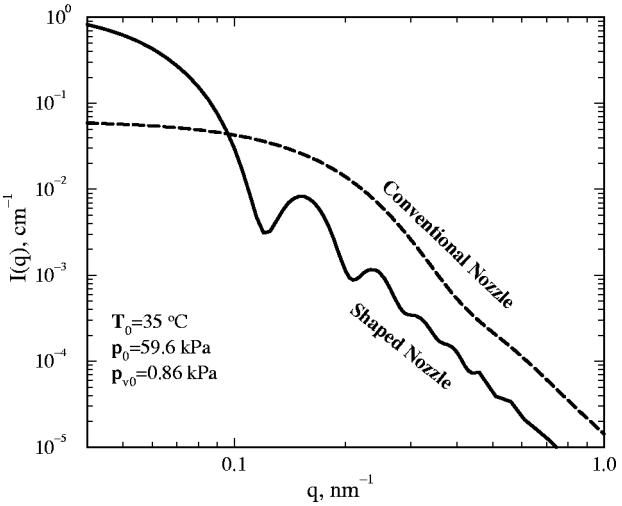

FIG. 3. The small angle neutron scattering spectrum predicted for the aerosol produced in the shaped nozzle (solid line) exhibits more structure and has a higher intensity intercept than the spectrum for the aerosol produced in the conventional nozzle (dashed line). The additional structure appears because the relative width of the size distribution $\sigma_r/\langle r\rangle$ is smaller in the shaped nozzle. The position of the first Bessel function minimum (Ref. 46) is inversely related to the average particle size. Thus, the first minimum in the spectrum for the aerosol from the shaped nozzle is at lower q.

The optics consist of a photomultiplier tube (PMT) with a 632.8 nm bandpass filter, and a 62.9 mm lens that focuses the scattered light onto the PMT. The PMT is powered by a high voltage power supply, and the output from the PMT is sent to a digital storage oscilloscope. Light scattering from the aerosol is compared to that from the carrier gas to calculate the relative scattering signal of the droplets and to detect any drift in the background.

2. Small angle neutron scattering experiments

To address the limitations inherent in light scattering, we use small angle neutron scattering (SANS) to measure the size distribution of the aerosols formed in the nozzle. Because the neutron wavelength ($\lambda\sim0.5$–2 nm) is less than the average particle radius $\langle r\rangle$, the scattering spectrum strongly depends on the momentum transfer wave vector q, where $q\propto(4\pi/\lambda)\sin(\theta/2)$ and θ is the scattering angle of the neutrons.[46] In the appropriate q range the key parameters of the size distribution can be determined by fitting the spectrum using only a weak assumption about the general shape of the size distribution. Figure 3 compares the scattering spectra corresponding to the D_2O aerosol size distributions shown in Fig. 2. Although the scattering intensity is proportional to the number density, and N is significantly lower for the aerosol formed in the shaped nozzles, the $\langle r^6\rangle$ dependence at low q ensures adequate signal strength. As expected, the scattering spectrum predicted for the aerosol formed in the shaped nozzle has more structure than the spectrum predicted for the aerosol formed in the conventional nozzle.

We conduct the aerosol SANS experiments using the NG7-SANS instrument at the National Institute for Standards and Technology (NIST). The neutron wavelength is $\lambda=0.8$ nm and the wavelength spread is $\Delta\lambda/\lambda=0.22$. The neutron beam is perpendicular to the aerosol stream and the scattered neutrons are detected by a two-dimensional detector. The experiments are completed at sample-to-detector distances (SDD) of 2.9 m or 1 m. SANS signals are relatively weak, and thus a larger (4 mm high, 12 mm wide, and 12.7 mm deep) viewing volume is used than in the light scattering experiments. The viewing volume is fixed and centered 7.0 cm downstream of the throat to give the droplets as much time as possible to grow. The nozzle is placed in an evacuated sample box, and the sapphire and silicon windows separating the sample box from the neutron guide and the detector tube are removed. For these experiments the residual gas pressure in the evacuated region was ~20 Pa. We alternate 30 min of sample measurements with 30 min of scattering from pure N_2 in order to monitor the level of the background closely. As long as the background does not drift, individual runs can be averaged. For many of the current experiments the cumulative backgrounds are 8.5–10 h long. Sample measurements are 30 min to 2 h long.

The $I(q)$ spectra are derived from the raw data in the following way. The two-dimensional intensity data are first corrected by subtracting the scattering signal from the nozzle flowing pure N_2. The corrected data are then adjusted for any nonuniformities in detector efficiency by dividing the intensities by those from a water sample on a pixel-by-pixel basis. The data are then placed on an absolute scale and bad detector pixels are masked. The absolute scale is determined by measuring the attenuated neutron flux reaching the detector during a beam center determination (direct beam measurement). Under our operating conditions, the two-dimensional scattering patterns are anisotropic because the speed of the droplets (400–500 m/s) is comparable to that of the cold neutrons (500 m/s), introducing a Doppler shift in the momentum of the neutrons that have a scattering component along the flow axis.[32,47] A modified version of the AVERAGE command in the standard NIST data reduction package,[48] AVERAGE/DOPPLER,[49] now corrects for the Doppler shift in the binning routine used to derive the averaged $I(q)$ spectra. The particle velocity used by the program is derived from the pressure trace measurements.

IV. RESULTS AND DISCUSSION

A. Thermodynamic state measurements

We first conducted pressure trace experiments with pure N_2 to characterize the assembled nozzle. As illustrated by the lowest pressure trace (solid gray line) in Fig. 4(a), our nozzle exhibits the key features required to separate nucleation from droplet growth, i.e., there is a well defined pressure minimum followed by a recompression and a second expansion. The initial expansion rate $d(A/A^*)_1/dx=0.043\,\mathrm{cm}^{-1}$ is reasonable, but the second expansion rate $d(A/A^*)_2/dx=0.031\,\mathrm{cm}^{-1}$ is larger than planned. Furthermore, the ~1 cm long nucleation zone is shorter and not as flat as desired. Thus, although nucleation and growth are separated, the nucleation rate, supersaturation, and temperature are not constant in the nucleation zone. Our situation is similar to that found in Schmitt *et al.*'s expansion cloud chamber,[36] and in

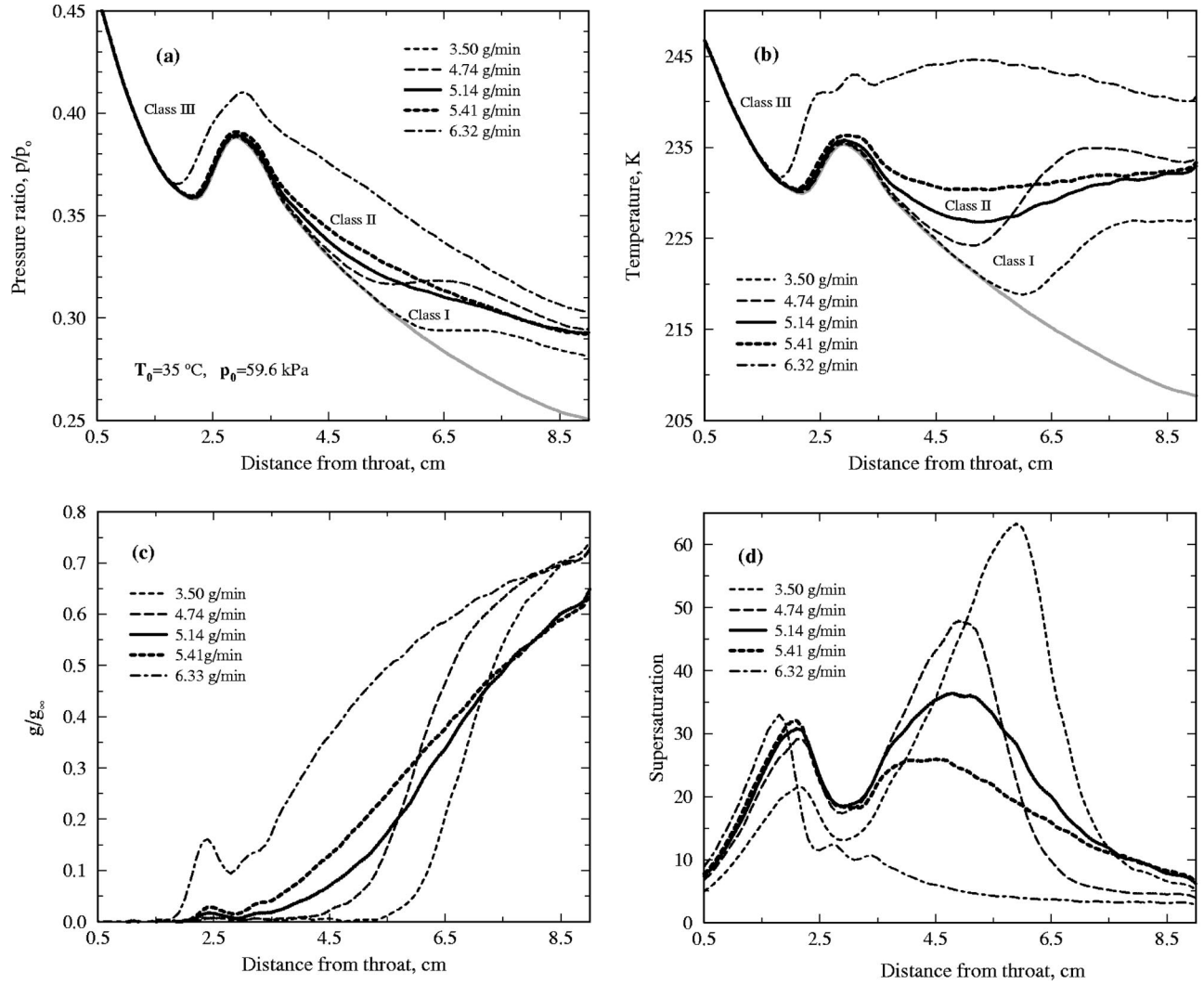

FIG. 4. The state of the supersonic flow as a function of position x in the nozzle is characterized in terms of (a) the measured pressure ratio p/p_0, (b) the temperature T, (c) the fraction of material condensed g/g_∞, and (d) the supersaturation S. The three flow rate classes are indicated in parts (a) and (b). The stagnation pressure and temperature are given in part (a).

the laminar diffusion flow tube[50–52] and can be treated in a similar manner. Finally, for the nozzle profile defined by the experimental pressure trace, the 1D model suggests that the final aerosol is bimodal unless condensation occurs either upstream or far downstream of the nucleation zone. The larger mode of the aerosol corresponds to the droplets that are formed in the controlled nucleation zone, while the smaller droplets come from a spontaneous burst of nucleation during the second expansion. Nevertheless, because the two nucleation events are separated in time, and the scattering intensity is proportional to $N\langle r^6\rangle$ in the small q region, the light scattering signal and most of the neutron scattering signal will be dominated by the large droplet mode.

TABLE I. The results of the pressure trace experiments are summarized in terms of the stagnation and onset conditions. In particular, the onset position, x_{on}, the onset pressure p_{on}, and the onset temperature T_{on} are shown. In all cases the stagnation pressure was $p_0=59.6$ kPa. The classification scheme is explained in the body of the text.

T_0, °C	$\dot{m}_v$, g/min	p_{v0}, Pa	x_{on}, cm	p_{on}, Pa	T_{on}, K	Class
35.0	3.27	546	5.99	162	218.1	I
	3.50	585	5.59	178	219.2	I
	4.06	678	5.14	213	221.9	I
	4.74	791	4.31	268	226.6	I
	5.14	858	3.06	333	235.5	II
	5.41	903	2.18	325	230.6	II
	5.81	970	2.00	351	231.0	III
	6.32	1056	1.82	386	231.7	III
	6.97	1163	1.50	442	234.6	III
45.0	6.93	1103	5.09	349	229.7	I
	7.92	1261	4.32	427	234.0	I
	9.47	1508	2.10	544	238.4	II

We then conducted pressure trace experiments with D_2O–N_2 gas mixtures to determine the D_2O concentrations corresponding to the best separation of nucleation and growth. The experiments started from a stagnation pressure of $p_0=59.6$ kPa and stagnation temperatures of $T_0=35.0$ °C and 45.0 °C. Table I summarizes all of the conditions investigated and classifies the experiments according to the location of the onset of condensation as well as the general shape of the condensing flow curve. Class I includes those cases where particle formation in the nucleation zone is negligible, and the aerosol is primarily formed during the second expansion. Class III encompasses the other extreme, where onset occurs distinctly upstream of the recompression.

Both class I and class III condensation events are similar to condensation in a conventional Laval nozzle. Class II condensation events correspond to the intermediate D_2O mass flow rates (or partial pressures) where we believe nucleation and growth are largely decoupled for the droplets formed in the nucleation zone. High stagnation temperatures and D_2O partial pressures were used throughout the experiments in order to maximize the volume fraction of condensate and, therefore, the neutron scattering signal. Our discussion focuses on the $T_0=35.0\,°C$ data, because these data are the most extensive. The $T_0=45.0\,°C$ data exhibit the same trends.

Figure 4(a) illustrates selected pressure traces measured for expansions starting from $T_0=35\,°C$. Figures 4(b)–4(d) show the profiles, derived from the pressure traces, for the temperature T, the fraction of D_2O condensed g/g_∞ (where $g_\infty=\dot{m}_v/\dot{m}_i$), and the supersaturation S. The supersaturation is calculated using the value of p_v derived from the pressure trace data and the equilibrium vapor pressure[53] for D_2O. Two cases of class I and class II condensation and one case of class III condensation are shown in each figure. Velocity profiles were also derived because the average droplet velocity is required to correctly interpret the SANS results. They are not shown here because they are essentially mirror images of the pressure profiles.

The class I condensation events are represented by the data at $\dot{m}_v=3.50$ and 4.74 g/min ($p_{v0}=585$, 791 Pa). We will first focus on the pressure trace at 3.50 g/min (short dashed line) because this is the cleanest example of a class I condensation event. In this experiment, p/p_0 and T both follow the isentrope closely until $x=5.5$ cm, more than 2.5 cm after the top of the recompression. The abrupt deviation in pressure and temperature, and the rapid increase in g/g_∞ to ~ 0.7, are reminiscent of a spontaneous condensation event in a conventional nozzle, i.e., almost all of the particles are formed in a rapid burst of nucleation and then grow rapidly, depleting the vapor and quenching nucleation. Furthermore, the supersaturation peak at $x\approx 6$ cm downstream of the throat is almost three times higher than the peak found in the nucleation zone. Although T is ~ 10 K lower for the second peak than the first, classical nucleation theory predicts that the nucleation rate corresponding to the second supersaturation maximum is four orders of magnitude higher than that for the first. Since classical nucleation theory predicts a stronger temperature dependence than observed experimentally,[37] this is at least a lower bound, and for a 10 K change in temperature the relative rates should be approximately correct. The second class I condensation curve, at $\dot{m}_v=4.74$ g/min, exhibits very similar behavior although the superaturation peaks are less disparate. Thus, the aerosol is probably bimodal and the scattering signals may be dominated by the larger droplet mode. This flow rate represents a transition between class I and class II condensation.

At the other extreme is the class III condensation event, corresponding to the experiment conducted at $\dot{m}_v=6.32$ g/min ($p_{v0}=1056$ Pa). At this flow rate, p/p_0 and T both deviate from the isentropic values about 1.7 cm downstream of the throat and the fraction of material condensed increases correspondingly. Thus, particle formation occurs well upstream of the nucleation zone and, up to the end of the first expansion, the picture is identical to condensation in a conventional nozzle. Because p/p_0 depends both on A/A^* and the heat released to the flow, it is difficult to visualize from the pressure data how the recompression, starting at $x\approx 2.2$ cm, effects the condensation process. The behavior of g/g_∞, is far more informative. In particular, the peak in g/g_∞ near $x\approx 2.4$ cm is close to the minimum pressure ratio in the nucleation zone. As the nozzle narrows, g/g_∞ starts to decrease and droplets evaporate rather than grow. At the end of the recompression, $x\approx 3$ cm, droplet growth resumes and g/g_∞ increases monotonically to the end of the nozzle where it reaches a maximum value of ~ 0.7. Like p/p_0, T depends both on the flow geometry and heat addition or removal due to droplet growth or evaporation. Thus, during the initial part of the recompression T increases before leveling off in a region where the heat absorbed by the evaporating aerosol exactly balances the increase in T due to recompression. On the downstream side of the recompression, T also remains relatively stable as the heat released by the growing droplets is balanced by the second expansion. Finally the supersaturation profile for this case contains only one significant peak, corresponding to the onset of condensation in the nozzle, and the aerosol will be unimodal.

The picture presented by the key variables raises the interesting prospect that in class III condensation events the recompression can process the aerosol so as to increase the average particle size and make the aerosol more monodisperse. Since the vapor pressure is highest above the smallest droplets, more material will evaporate from small droplets than from large ones. If the smallest droplets vanish completely during the recompression, condensation on the remaining droplets during the second expansion should deplete the vapor enough to prevent further droplet formation. Thus, the shaped nozzle could hasten the natural process of Ostwald ripening.[54] This effect should be stronger the closer onset occurs to the recompression, because the newly formed droplets have less time to grow and are therefore more likely to evaporate.

We now consider the best conditions for the desired class II condensation behavior (solid and heavy dashed lines). The experiment at 5.41 g/min ($p_{v0}=903$ Pa) is an upper bound on this class since the pressure trace starts to deviate from the isentropic expansion just before the end of the nucleation zone. The deviation is, however, weak and p/p_0 follows the shape of the isentrope beyond the peak of the recompression and only clearly separates from the isentrope at $x=3.5$ cm. Finally, the experiment at $\dot{m}_v=5.14$ g/min ($p_{v0}=858$ Pa), is our best example for class II condensation. Within experimental error, p/p_0 and T follow their respective isentropes exactly until the peak of the recompression, where they deviate slowly from the isentropic values. This behavior is consistent with droplet formation that is maximized in the nucleation zone, cut off rapidly by the recompression, and the remaining phase transition is accomplished by droplet growth. The behavior of g/g_∞ also confirms that class II condensation is qualitatively different from the other cases. For example, the increase in g/g_∞ is much slower and at x

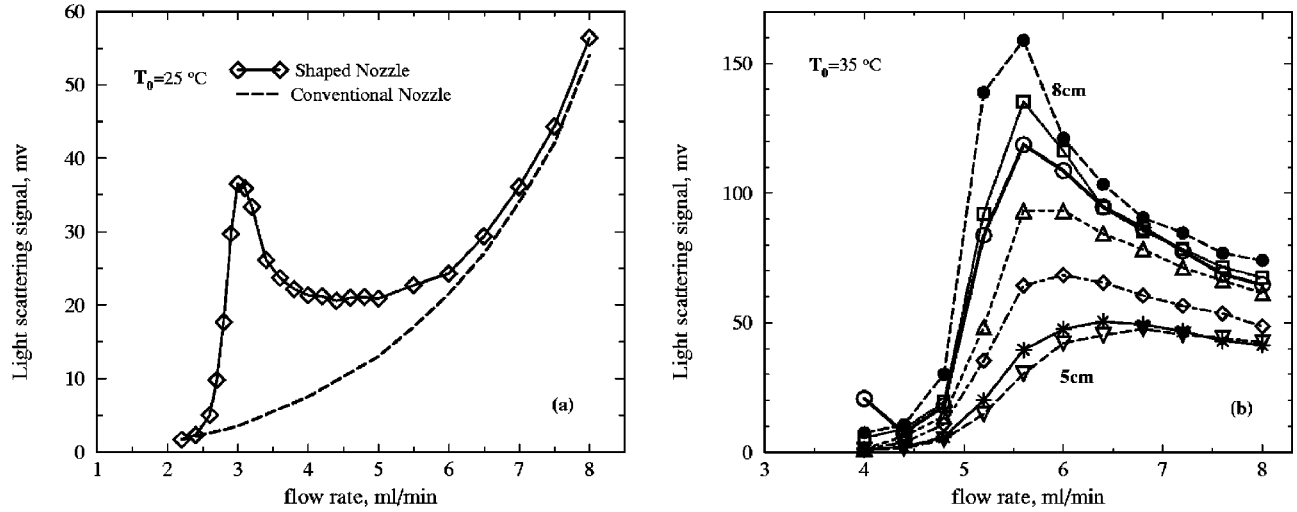

FIG. 5. The light scattering signal in the shaped nozzle approaches that for a conventional nozzle at the operating extremes but exhibits unusual structure at the intermediate flow rates where nucleation rates are reduced and the droplets grow to larger size. (a) At $T_0=25\,^{\circ}\mathrm{C}$, the data in the shaped nozzle correspond to a position $x=8$ cm downstream of the throat. In the conventional nozzle, the general trend of the flow rate dependence of the scattering signal is inferred from the results of Stein and Wegener (Ref. 13). (b) At $T_0=35\,^{\circ}\mathrm{C}$, each line joins the light intensity measurements taken at a fixed position. The top and bottom curves are labeled and correspond to $x=8$ and 5 cm downstream of the throat, respectively. Intermediate curves are spaced at 0.5 cm intervals. The structure in the light scattering signal is more pronounced further downstream in the nozzle because the droplets have had more time to grow.

$=9$ cm the value is distinctly lower than for the other experiments. Although g/g_∞ can be as low as 0.6 at the exit of a conventional nozzle for experiments that start under similar stagnation conditions, it always increases monotonically as g_∞ decreases.[55] Finally, Fig. 4(d) illustrates the major weakness of the current nozzle design. For both class II condensation cases, there is a significant supersaturation peak during the second expansion that occurs at a temperature close to that in the nucleation zone. Thus, although we have separated nucleation from growth for the particles formed in the nucleation zone, the final aerosol formed under these conditions is bimodal.

B. Light scattering validation

Light scattering experiments were conducted starting from three stagnation temperatures: $T_0=25.0$, 35.0, and 45.0 °C. The results obtained at different T_0 are qualitatively similar for the range of flow rates studied, and here we present the data for $T_0=25.0$ and 35.0 °C. Since the experiments were conducted quickly to conserve D_2O, the true mass flow rates were not measured. Thus, the results are all presented in terms of the volumetric flow rate reading from the peristaltic pump rather than the true mass flow rate.

Figure 5(a) presents the relative light scattering intensity as a function of the D_2O flow rate at $x\approx 8$ cm for $T_0=25.0\,^{\circ}\mathrm{C}$. In a continuously expanding nozzle where condensation is not controlled, the light scattering signal increases monotonically[16] with the flow rate, as indicated qualitatively by the dashed line. This behavior can also be inferred from the values of N and $\langle r\rangle$ reported by Stein and Wegener[13] and is predicted by modeling. In contrast, the relative light scattering signal in the shaped nozzle has a complex structure. Starting from the lowest flow rates, the light scattering signal increases rapidly and peaks near a flow rate of 3 ml/min. As the flow rate continues to increase, the light scattering signal suddenly drops to a plateau in the flow rate range from 3.5 ml/min to 6 ml/min. When the flow rate increases above 6 ml/min, I_0 begins to increase in a manner consistent with a conventional nozzle. We believe that this complex behavior arises because near the flow rate of 3 ml/min, nucleation and growth are decoupled and light is scattered from a smaller number of larger droplets.

Figure 5(b) shows similar data for $T_0=35.0\,^{\circ}\mathrm{C}$, but now the detector position is also varied. The top curve corresponds to scattering measured at $x=8$ cm and the lower curves correspond to moving the observation point upstream

TABLE II. The conditions used to generate the nanodroplets corresponding to the spectra in Fig. 7. The expansions in the conventional (Ref. 56) nozzle (A) and the shaped nozzle (E) both started from $p_0=59.6$ kPa and $T_0=35.0\,^{\circ}\mathrm{C}$. Nozzle A has a constant expansion rate of $d(A/A^*)/dx=0.048\,\mathrm{cm}^{-1}$. In the region of onset, nozzle E had an expansion rate of $d(A/A^*)/dx=0.043\,\mathrm{cm}^{-1}$. The table compares the initial flow rates of the condensible $\dot{m}_v$ (p_{v0}), the onset conditions (x_{on}, p_{on}, T_{on}), and the location of the viewing volume x_{view}, and the best fit parameters to a log-normal size distribution (mean particle radius, $\langle r\rangle$; the width of distribution, $\ln\sigma$; and the droplet number concentration, N) derived by fitting the SANS spectra.

Nozzle	$\dot{m}_v$, g/min	p_{v0}, Pa	x_{on}, cm	p_{on}, Pa	T_{on}, K	x_{view}, cm	$\langle r\rangle$, nm	$\ln\sigma$	N, cm^{-3}
A	7.40	1197	2.00	419	228.8	5.60	9.68	0.218	4.70×10^{11}
E	6.97	1163	1.50	442	234.6	7.00	13.84	0.197	1.57×10^{11}

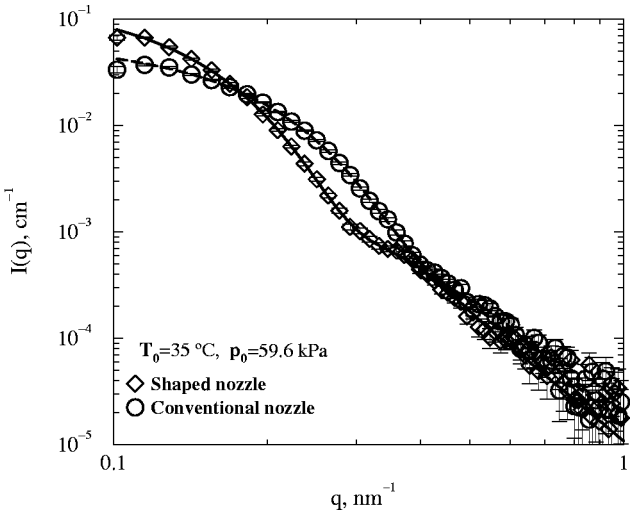

FIG. 6. The scattering spectrum for the aerosol formed in the conventional nozzle (Ref. 56) was measured 5.6 cm downstream of the throat and 3.6 cm downstream of the onset of condensation. By this point, the aerosol was no longer evolving and the fraction of material condensed had stabilized at $g/g_\infty \sim 0.7$. The scattering spectra from the aerosol formed in the shaped nozzle was measured 7 cm downstream of the throat and 5.5 cm downstream of the onset of condensation. In this case, the droplets in the viewing volume were still growing. The flow rate of D_2O was about 6% lower in the shaped nozzle experiment than the conventional nozzle experiment. Nevertheless, the relative positions of the first Bessel function minimum (Ref. 46) shows that the aerosol formed in the shaped nozzle has a larger average droplet size.

in 0.5 cm increments. As the observation region moves closer to the throat, the scattering signal decreases because the particles have not had as much time to grow and are, therefore, smaller. Downstream of $x=5.5$ cm, all of the light scattering curves have a peak near 5.6 ml/min similar to the one found for the 25 °C data near 3 ml/min. Although these experiments are only semiquantitative, they confirm that operating conditions exist under which nucleation and growth are decoupled in the shaped nozzle.

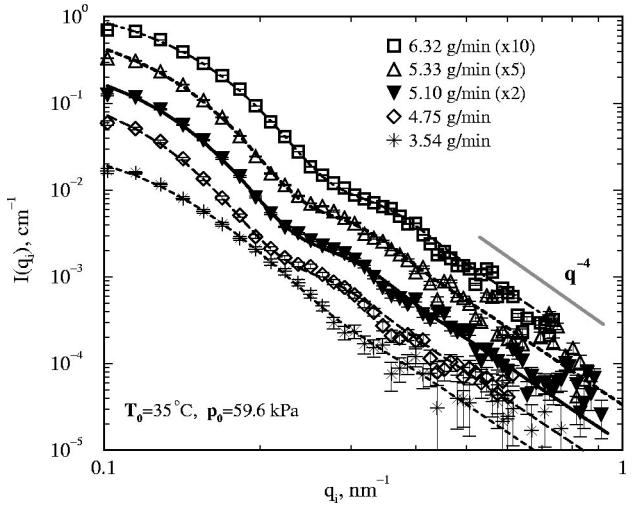

FIG. 7. The SANS spectra for five experiments with initial conditions corresponding to class I through class III condensation. The condensible mass flow rates $\dot{m}_v$ are close to those experiments presented in Figs. 4(a)–4(d). For clarity, the spectra corresponding to the two lowest flow rates are shown at their true absolute intensity. The spectra corresponding to higher flow rates have been offset by factors of 2, 5, and 10, respectively.

C. Aerosol SANS experiments

Finally, we conducted aerosol SANS experiments using the shaped nozzle. Again we focus on the results of experiments starting from $T_0=35.0$ °C.

We start by directly comparing the spectrum of an aerosol formed in the shaped nozzle to one formed in a conventional nozzle. The conditions under which each aerosol was formed are summarized in Table II. Figure 6 shows that the spectrum for the shaped nozzle aerosol has a distinct shoulder rather than an inflection point in the region $0.3<q<0.4\,\mathrm{nm}^{-1}$ and the value of I_0 is larger by a factor of 2. Both aerosols are unimodal because the flow rate in the shaped nozzle is high enough that this is a class III condensation event. The size distribution parameters presented in Table II are the best fit parameters to log-normal distributions. We see that the aerosol produced in the shaped nozzle has a number density that is a factor of three lower and an average particle size that is 30% larger than the aerosol formed in the conventional nozzle, even though the condensible mass flow rate through the shaped nozzle is somewhat lower.

Figure 7 presents the SANS spectra where the flow rates most closely match those in Fig. 4. When the D_2O mass flow rate is 4.75 g/min or above, the spectra all have a distinct shoulder in the region of the Bessel function minimum[46] ($0.2<q<0.3\,\mathrm{nm}^{-1}$). The shoulder is followed by a q^{-4} Porod decay, characteristic of scattering by homogeneous spherical particles.[46] At lower flow rates, the shoulder vanishes although an inflection point remains, and beyond the inflection point the intensity again falls off as q^{-4}. As the initial condensible flow rate increases from 3.54 g/min to 4.75 g/min, the inflection point moves to lower q consistent with an increase in the average particle size. In contrast, at flow rates above 4.75 g/min the shoulder shifts to higher q with increasing $\dot{m}_v$ and, thus, the average droplet size is decreasing.

We fit each spectrum assuming a unimodal aerosol with a log-normal size distribution of droplets and derive the mean droplet radius, $\langle r\rangle$, the width of distribution, $\ln\sigma$, and the number concentration of droplets, N. Although we believe that the aerosol is often bimodal, this preliminary analysis of the SANS data do not justify such a complex fitting procedure. One problem with the current data set is that the spectra are smeared because the droplets are still growing across the 12 mm wide viewing volume. Furthermore, in this work we are primarily interested in the large particle mode and this mode contributes the most to the scattering intensity at low q. Table III summarizes the droplet size distribution parameters derived from the spectral fits under these assumptions, as well as values for the radius of gyration R_G and the intensity intercept I_0 derived from a Guinier analysis.[46,57] For our polydisperse droplets, the linear region of the Guinier plots[57] extends up to $q^2 \approx 5.5\times10^{-6}\,\mathrm{nm}^{-2}$, corresponding to an upper bound of $qR_G<3.5$. For a relative polydispersity of ~20%, $\langle r\rangle$ should be close[58] to R_G, and the values in Table III confirm this.

TABLE III. The conditions of the aerosol SANS experiments are summarized along with the parameters of the log-normal aerosol size distributions determined by fitting the SANS spectra. The radius of gyration R_G and the intercept I_0 were determined by a Guinier analysis.

T_0, °C	$\dot{m}_v$, g/min	p_{v0}, Pa	$\langle r\rangle$, nm	$\ln\sigma$	N, cm^{-3}	R_G, nm	I_0, cm^{-1}
35.0	3.19	533	10.0	0.350	3.64×10^{10}	13.5	1.46×10^{-1}
	3.54	592	13.6	0.280	2.99×10^{10}	15.4	1.70×10^{-1}
	4.02	671	18.8	0.228	2.16×10^{10}	18.3	1.87×10^{-1}
	4.75	793	18.7	0.200	4.07×10^{10}	18.1	2.10×10^{-1}
	5.10	851	17.7	0.194	5.56×10^{10}	17.2	2.02×10^{-1}
	5.33	890	17.7	0.190	6.59×10^{10}	16.8	2.08×10^{-1}
	5.83	973	16.7	0.193	8.81×10^{10}	15.7	1.15×10^{-1}
	6.32	1055	15.2	0.193	11.24×10^{10}	14.7	4.06×10^{-2}
	6.97	1163	13.8	0.197	15.70×10^{10}	13.7	1.51×10^{-2}
45.0	7.02	1117	19.5	0.287	1.87×10^{10}		
	8.00	1274	21.0	0.243	2.72×10^{10}		
	9.60	1528	20.0	0.223	5.06×10^{10}		

Figure 8 compares the values of I_0 derived from the Guinier analysis to those deduced from the size distribution parameters using

$$I_0=\frac{16\pi^2}{9}\Delta\rho^2 N\langle r^6\rangle, \tag{7}$$

where $\Delta\rho^2$ is the scattering length density for D_2O and $\langle r^6\rangle=\langle r\rangle^6\exp[18(\ln\sigma)^2]$ for a log-normal size distribution. The values of I_0 derived from Eq. (7) generally lie above the values derived from the Guinier analysis, but the trends are the same. To directly compare these values of I_0 to those measured by light scattering, we scaled the maximum light scattering intensity to correspond to the maximum SANS intensity. We also scaled the flow rate by a single factor (0.89 g/ml) so that the flow rate at $I_{0,\max}$ from light scattering lined up with $I_{0,\max}$ from SANS. When all of the remaining points were scaled using these two factors, the agreement between the light scattering measurements and the quantitative SANS results is quite good.

Figure 9 shows the variation of $\langle r\rangle$, R_G, and N as a function of the mass flow rate. Both $\langle r\rangle$ and R_G have a maximum at $\dot{m}_v\approx4$ g/min, and this in turn, corresponds to the minimum in N. For flow rates less than 5.5 g/min, this behavior is readily understood by looking back at the thermodynamic data, especially the temperature and supersaturation profiles in Figs. 4(b) and 4(d). At the lowest flow rates, $\dot{m}_v<4$ g/min, the number of droplets formed in the nucleation zone is small and the scattering signal primarily reflects the particles formed by the nucleation event in the second expansion. As the flow rate increases above 4 g/min, the supersaturation in the nucleation zone increases steadily although the temperature profiles in this region are unchanged. The nucleation rate in the nucleation zone, and the number of particles that comprise the large mode of the aerosols must therefore increase. Because more particles are formed in the nucleation zone, the supersaturation after the recompression peak decreases and the droplets cannot grow as large before

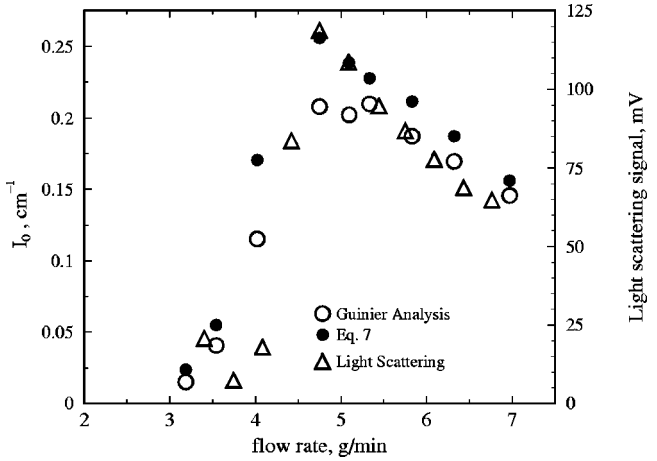

FIG. 8. Over the entire range of condensible flow rates, the values of I_0 derived from fits to the full SANS spectra [Eq. (7)] are in good agreement with those derived from Guinier analysis (Refs. 46, 57). Furthermore, the independent measurement of I_0 from the rescaled light intensity signals, are also in reasonable agreement. The data for both SANS and light scattering was obtained at $T_0=35$ °C.

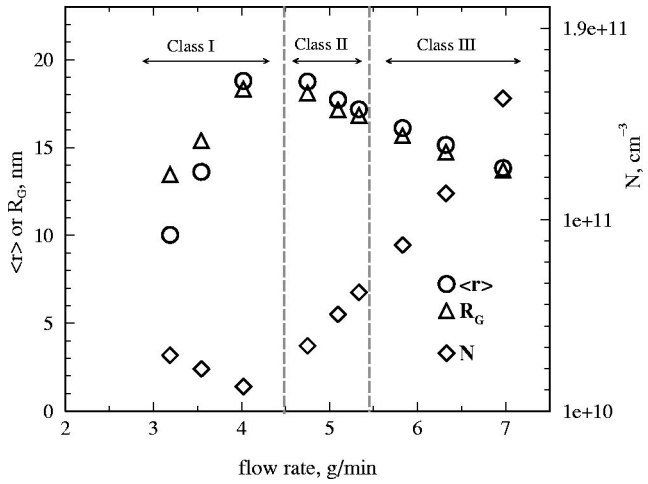

FIG. 9. The average particle size $\langle r\rangle$, the radius of gyration R_G, and the number density of the aerosol N are plotted as a function of the condensible mass flow rate. The size distribution parameters are obtained from the spectra measured in the 12 mm wide viewing volume centered at $x=7$ cm. The aerosol with the largest droplet size and lowest number density is formed in the transition from class I to class II condensation where $\dot{m}_v\sim4$ g/min. Experiments were performed at $T_0=35$ °C.

TABLE IV. This table summarizes the location x_{max}, and conditions $p_{v,max}$, S_{max}, and T_{max}, corresponding to the maximum nucleation rate J_{max} for the three experiments where nucleation and growth are decoupled. The number concentration N_{corr} has been corrected for the difference in gas density between the viewing volume and the nucleation zone. The characteristic time Δt was calculated as described in the text.

$\dot{m}_v$, g/min	x_{max}, cm	$p_{v,max}$, Pa	T_{max}, K	S_{max}	N_{corr}, cm^{-3}	Δt, s	J_{max}, $cm^{-3}\,s^{-1}$
4.74	2.10	279	230.1	29.2	4.68×10^{10}	1.32×10^{-5}	4.32×10^{15}
5.14	2.10	303	230.3	30.8	6.47×10^{10}	1.39×10^{-5}	4.62×10^{15}
5.41	2.08	320	230.4	32.0	7.67×10^{10}	1.43×10^{-5}	6.01×10^{15}

they reach the observation region, and hence the average droplet size decreases.

For the highest flow rates ($\dot{m}_v > 5.5$ g/min), droplets are formed upstream of the nucleation zone. Under these conditions one would expect N to decrease or stay relatively constant[13] and $\langle r \rangle$ to increase as the mass flow rate increased. We observe the opposite trend and believe that this is further evidence that the recompression processes the aerosol, evaporating the smallest droplets and letting the remaining droplets grow larger. Based on the 25.0 °C light scattering data, we would need to further increase the flow rates at $T_0 = 35.0$ °C to reverse this trend.

D. Estimates of the nucleation and growth rates

When nucleation and droplet growth are separated, we can estimate nucleation rates as $J(S,T) = N/\Delta t$. The value of N comes from the SANS measurement assuming that the observed number density corresponds to the large mode of the aerosol and that these droplets all form in the nucleation zone. We must also correct the observed number density for the ~15% difference in gas density between the viewing volume and the nucleation zone. Within the nucleation zone the gas density changes by less than 2%–3% and is ignored.

The second step is to analyze the experimentally determined supersaturation and temperature profiles in the controlled nucleation region to determine the time, Δt, over which most of the droplets comprising the large mode of the aerosol are formed. As in laminar flow tube experiments,[50–52] we assume that the ratio of the maximum nucleation rate J^{max} to the particle production rate $\int J dV$ is the same for the experiments as that predicted by a reasonable nucleation rate theory. If this is true then,

$$\frac{J^{max}_{exp}}{\int J_{exp} dV} = \frac{J^{max}_{theory}}{\int J_{theory} dV} = f. \tag{8}$$

The quantity f has units of cm^{-3} and, thus, $V_{J,max} = 1/f$ is the characteristic volume corresponding to the maximum nucleation rate. We confirmed the observation[50,51] that the value of $V_{J,max}$ is quite insensitive to the nucleation rate expression chosen. In fact, for our experiments, the value predicted by the classical nucleation theory differed from that predicted by the Reiss, Katz, Kegel theory[59] by less than 1%. From the characteristic nucleation volume and the volumetric flow rate in the nucleation zone $\dot{V}$ we can then estimate the characteristic time for nucleation Δt as

$$\Delta t = \frac{V_{J,max}}{\dot{V}} = \frac{\rho_g V_{J,max}}{\dot{m}}, \tag{9}$$

where ρ_g is the gas density in the nucleation zone and $\dot{m} = \dot{m}_v + \dot{m}_i$ is the total mass flow rate through the nozzle.

Based on all of the experimental evidence, D_2O mass flow rates between 4.74 g/min and 5.41 g/min (791 Pa $\leqslant p_{v0} \leqslant$ 903 Pa) provide the best decoupling between nucleation and growth. Using the formalism described above, and the experimental supersaturation and temperature profiles, we derived values for $J^{max}_{exp}(S,T)$ for the three experiments in this flow rate range. We assume that J_{exp} is maximized at the same S and T as J_{theory}, and these are the values reported in Table IV. Finally, because the nucleation rates are close to isothermal, we can estimate the number of molecules in the critical cluster n^* using the nucleation theorem[38,60] as

$$\left[\frac{d \ln J}{d \ln S}\right]_T \approx n^* - 1. \tag{10}$$

For this data set, we find $n^* \approx 5$.

We can also estimate the particle growth rate in the nozzle. From the SANS data we know the average size of the droplets in the viewing volume centered at $x = 7$ cm. As demonstrated in Fig. 8, the relative behavior of I_0 from light scattering closely matches that derived from SANS. We can therefore use the $I_0(x)$ data in Fig. 5(b) to estimate relative droplet size if we assume that (1) the number of particles in the large particle mode does not change during the second

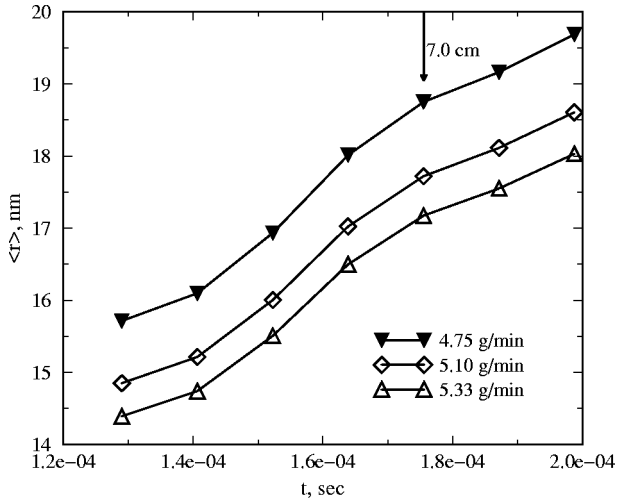

FIG. 10. The change in average droplet size as a function of time was deduced from the light scattering data in Fig. 5(b), the gas stream velocity, the SANS measurement at $x = 7$ cm, and Eq. (11). The times are all relative to $t = 0$ s at the throat. The three flow rates correspond to class II condensation and the transition to class I. The arrow marks the location where the SANS measurements were made.

expansion and (2) the relative width of the distribution ($\ln \sigma$) is constant. With these assumptions, changes in $I_0(x)$ are related to changes in $\langle r(x)\rangle$ by

$$\frac{I_0(x)}{I_0(7.0)} = \frac{N\langle r^6(x)\rangle}{N\langle r^6(7.0)\rangle} \approx \frac{\langle r(x)\rangle^6}{\langle r(7.0)\rangle^6}. \tag{11}$$

The droplet velocities come from the pressure trace experiments, and, thus, we deduce the time evolution of the droplet size.

Figure 10 illustrates the particle size as a function of time for three different values of p_{v0} where $t=0$ corresponds to the position at the throat. In each case droplet growth slows near the nozzle exit due, in part, to the growth of the small particles formed during the second nucleation burst. Approximate growth rates can be derived by numerically differentiating these curves. For example, at $x=7.0$ cm and $\dot{m}_v=5.10$ g/min, $\langle r\rangle=17.7$ nm and $d\langle r\rangle/dt \approx 4.2\times10^4$ nm/s. From the thermodynamic data in Figs. 4(a) and 4(d), the corresponding temperature and supersaturation are $T=230.3$ K and $S=14.8$.

One assumption that we have made in all of our analysis is that the flow in the nozzle is one dimensional. A nozzle such as ours is inherently two dimensional because the weak shocks that recompress the flow take time to propagate from the walls to the centerline. Different stream tubes therefore experience different supersaturation histories and so the region where nucleation is significant cannot be uniform across the nozzle.[22,25] We are starting to explore this problem in more detail in order to refine our estimates of $J(S,T)$.

V. SUMMARY AND CONCLUSIONS

We have built a shaped nozzle that decouples droplet nucleation and growth in a supersonic expansion. We characterized the nozzle and determined the optimal operating conditions using thermodynamic state measurements and light scattering experiments. Under a limited range of conditions ($791\ \text{Pa} \leqslant p_{v0} \leqslant 903\ \text{Pa}$), that we called class II condensation, the measured pressure profiles, the deduced temperature profiles, the amount of condensible, and the supersaturation profiles are consistent with nucleation localized in a $\sim$1 cm long region of the nozzle. The decoupling of nucleation and growth is not complete in the nozzle used here because a second nucleation burst in the second expansion region often results in a bimodal aerosol. The two other condensation classes correspond to condensible pressures that are too high (class III) or too low (class I). In these cases, spontaneous nucleation outside the nucleation zone dominates particle formation and the aerosol can be unimodal. In class III condensation, flow recompression may enhance the natural process of Ostwald ripening by evaporating the smallest droplets during the recompression and only growing the remaining droplets during the second expansion.

We used SANS to directly measure the size distribution parameters of the aerosols formed in the shaped nozzle. The SANS experiments confirmed the findings of the pressure trace and light scattering measurements for the conditions corresponding to the best decoupling of nucleation and growth. Assuming that for class II condensation the small particle mode formed during the second expansion contributes little to the SANS spectra in our q range, we estimated the number density N of particles formed in the controlled nucleation zone. We then analyzed the supersaturation and temperature profiles to determine the time interval Δt over which droplet formation is significant. From N and Δt we obtained the first direct measurements of the nucleation rate $J(S,T)$ in a supersonic nozzle. By analyzing the change in I_0 from the light scattering data with the position we also obtained the first independent estimates of the growth rate of droplets in a supersonic nozzle.

ACKNOWLEDGMENTS

The authors thank A. Khan for assisting in the light scattering experiments and U. Dieregsweiler for providing the conventional nozzle data in Fig. 6 and Table II. We thank J. Wölk for assistance with the preliminary nozzle design. We thank our local NIST contacts J. Barker and C. Glinka for their assistance in our experiments. We also gratefully acknowledge the other members of "the SANS dream team," C. Heath, J. Wölk, A. Khan, U. Dieregsweiler, and G. Wilemski for their active participation in the SANS experiments and useful discussions. This work was supported by the National Science Foundation, Division of Chemistry under Grants Nos. CHE-9729274, CHE-0089136, and by the Donors of the Petroleum Research Fund administered by the American Chemical Society. The work is based on activities supported by the National Science Foundation under Agreement No. DMR-9986442.

[1] P. P. Wegener, *Nonequilibrium Flows, Part I*, Vol. 1, in *Gasdynamics*, edited by P. P. Wegener (Dekker, New York, 1969), Chap. 4, p. 163.
[2] D. E. Kinnison, K. E. Grant, P. S. Connell, D. A. Rotman, and D. J. Wuebbles, J. Geophys. Res., [Solid Earth] **99**, 25705 (1994).
[3] A. J. White and J. B. Young, AIAA J. **9**, 579 (1993).
[4] A. J. White and J. B. Young, Philos. Trans. R. Soc. London, Ser. A **354**, 59 (1996).
[5] D. W. Oxtoby, J. Phys.: Condens. Matter **4**, 7627 (1992).
[6] I. J. Ford, Phys. Rev. E **56**, 5615 (1997).
[7] G. M. Pound, J. Phys. Chem. Ref. Data **1**, 119 (1972).
[8] S. Kotake and I. I. Glass, Prog. Aerosp. Sci. **19**, 129 (1981).
[9] R. H. Heist and H. He, J. Phys. Chem. Ref. Data **23**, 781 (1994).
[10] K. Oswatitsch, Z. Angew. Math. Mech. **22**, 1 (1942).
[11] P. P. Wegener and A. A. Pouring, Phys. Fluids **7**, 352 (1964).
[12] P. G. Hill, J. Fluid Mech. **25**, 593 (1966).
[13] G. D. Stein and P. P. Wegener, J. Chem. Phys. **46**, 3685 (1967).
[14] H. L. Jaeger, E. J. Willson, P. G. Hill, and K. C. Russell, J. Chem. Phys. **51**, 5380 (1969).
[15] D. B. Dawson, E. J. Willson, P. G. Hill, and K. C. Russell, J. Chem. Phys. **51**, 5389 (1969).
[16] J. A. Clumpner, J. Chem. Phys. **55**, 5042 (1971).
[17] D. Barschdorff, Phys. Fluids **18**, 529 (1975).
[18] B. J. C. Wu, P. P. Wegener, and G. D. Stein, J. Chem. Phys. **68**, 308 (1978).
[19] B. J. C. Wu, P. P. Wegener, and G. D. Stein, J. Chem. Phys. **69**, 1776 (1978).
[20] P. P. Wegener, J. A. Clumper, and B. J. C. Wu, Phys. Fluids **15**, 1869 (1972).
[21] B. E. Wyslouzil, G. Wilemski, M. G. Beals, and M. B. Frish, Phys. Fluids **6**, 2845 (1994).
[22] S. Adam and G. H. Schnerr, J. Fluid Mech. **348**, 1 (1997).
[23] Y. Okada, S. Isomura, K. Ashime, and K. Takeuchi, Appl. Phys. B: Lasers Opt. **B67**, 247 (1998).
[24] B. E. Wyslouzil, C. H. Heath, J. L. Cheung, and G. Wilemski, J. Chem. Phys. **113**, 7317 (2000).

[25] G. Lamanna, Ph.D. thesis, Eindhoven University of Technology, 2000.
[26] T. Pierce, P. M. Sherman, and D. D. McBride, Astronaut Acta **16**, 1 (1971).
[27] G. D. Stein and C. A. Moses, J. Colloid Interface Sci. **39**, 504 (1972).
[28] C. A. Moses and G. D. Stein, J. Fluids Eng. **100**, 311 (1978).
[29] G. Cinar, B. S. Yilbas, and M. Sunar, Int. J. Multiphase Flow **23**, 1171 (1997).
[30] J. B. Young, PCH, PhysicoChem. Hydrodyn. **3**, 57 (1982).
[31] B. E. Wyslouzil, J. L. Cheung, G. Wilemski, and R. Strey, Phys. Rev. Lett. **79**, 431 (1997).
[32] B. E. Wyslouzil, G. Wilemski, J. L. Cheung, R. Strey, and J. Barker, Phys. Rev. E **60**, 4330 (1999).
[33] C. H. Heath, K. A. Streletzky, J. Wölk, B. E. Wyslouzil, and R. Strey, *Nucleation and Atmospheric Aerosols*, edited by B. Hale and M. Kulmala (AIP, New York, 2000), p. 59.
[34] C. H. Heath, K. A. Streletzky, B. E. Wyslouzil, and G. Wilemski, *Nucleation and Atmospheric Aerosols*, edited by B. Hale and M. Kulmala (AIP, New York, 2000), p. 63.
[35] J. R. Turner, T. T. Kodas, and S. K. Friedlander, J. Chem. Phys. **88**, 457 (1988).
[36] G. W. Adams, J. L. Schmitt, and R. A. Zalabsky, J. Chem. Phys. **81**, 5074 (1984).
[37] R. Strey, P. Wagner, and T. Schmeling, J. Chem. Phys. **84**, 2325 (1986).
[38] R. Strey, P. Wagner, and Y. Viisanen, J. Phys. Chem. **98**, 7748 (1994).
[39] F. Peters and B. Paikert, Exp. Fluids **7**, 521 (1989).
[40] F. Peters and T. Rodemann, Exp. Fluids **24**, 300 (1998).
[41] C. C. M. Luijten, K. J. Bosschaart, and M. E. H. van Dongen, J. Chem. Phys. **106**, 8116 (1997).
[42] C. C. M. Luijten, O. D. E. Baas, and M. E. H. van Dongen, J. Chem. Phys. **106**, 4152 (1997).
[43] H. W. Liepmann and A. Roshko, *Elements of Gasdynamics* (Wiley, New York, 1957).
[44] F. F. Abraham, *Homogeneous Nucleation Theory* (Academic, New York, 1974).
[45] J. Wölk, Ph.D. thesis, University of Cologne, 2001.
[46] O. Glatter and O. Kratky, *Small Angle X-Ray Scattering* (Academic, London, 1982).
[47] G. Wilemski, Phys. Rev. E **61**, 557 (2000).
[48] National Institute of Standards and Technology, Center for Neutron Research, *SANS Data Reduction and Imaging Software*, June 1999.
[49] J. Barker (private communication).
[50] P. E. Wagner and M. Anisimov, J. Aerosol Sci. **24s1**, 103 (1993).
[51] K. Hämeri, M. Kulmala, E. Krissinel, and G. Kodenyov, J. Chem. Phys. **105**, 7683 (1996).
[52] V. B. Mikheev, N. S. Laulainen, S. E. Barlow, M. Knott, and I. Ford, J. Chem. Phys. **113**, 3704 (2000).
[53] P. G. Hill, R. D. C. McMillan, and V. Lee, J. Phys. Chem. Ref. Data **11**, 1 (1982).
[54] R. Boistelle and J. P. Astier, J. Cryst. Growth **168**, 14 (1988).
[55] C. H. Heath, Ph.D. thesis, Worcester Polytechnic Institute, 2001.
[56] U. M. Dieregsweiler, Master thesis, Worcester Polytechnic Institute, 2001.
[57] In the limit of $q \to 0$, the Guinier regime, the scattering intensity varies as $I = I_0 \exp(-q^2 R_G^2/3)$. Thus, a plot of $\ln I$ vs q^2 is linear with slope $-R_G^2/3$ and intercept $\ln I_0$.
[58] The radius of gyration R_G is defined as $R_G^2 = (3/5)\langle r^8\rangle/\langle r^6\rangle$. For a log-normal size distribution $\langle r^n\rangle = \langle r\rangle^n \exp[(n^2/2)(\ln \sigma)^2]$, and $R_G^2 = (3/5) \times \langle r\rangle^2 \exp(14(\ln \sigma)^2)$. For $\ln \sigma = 0.2$, $R_G \approx 1.03\langle r\rangle$.
[59] H. Reiss, W. K. Kegel, and J. L. Katz, Phys. Rev. Lett. **78**, 4506 (1997).
[60] D. Kashchiev, J. Chem. Phys. **76**, 5098 (1982).